Physics of the Earth and Planetary Interiors 334 (2023) 106973

Contents lists available at ScienceDirect

Physics of the Earth and Planetary Interiors

journal homepage: www.elsevier.com/locate/pepi

A previously unidentified fault revealed by the February 25, 2022 (Mw 6.1) Pasaman Earthquake, West Sumatra, Indonesia

Pepen Supendi [a,b,*], Nicholas Rawlinson [a], Bambang Setiyo Prayitno [b], Dimas Sianipar [b], Andrean Simanjuntak [b], Sri Widiyantoro [c,d], Kadek Hendrawan Palgunadi [e], Andri Kurniawan [f], Hasbi Ash Shiddiqi [g], Andri Dian Nugraha [c], David P. Sahara [c], Daryono Daryono [b], Rahmat Triyono [b], Suko Prayitno Adi [b], Dwikorita Karnawati [b], Gatut Daniarsyad [b], Suaidi Ahadi [b], Iman Fatchurochman [b], Suci Dewi Anugrah [b], Nova Heryandoko [b], Ajat Sudrajat [b]

[a] Department of Earth Sciences – Bullard Labs, University of Cambridge, Cambridge CB30EZ, United Kingdom
[b] Agency for Meteorology, Climatology, and Geophysics, Jakarta 10720, Indonesia
[c] Global Geophysics Research Group, Faculty of Mining and Petroleum Engineering, Institut Teknologi Bandung, Bandung 40132, Indonesia
[d] Faculty of Engineering, Maranatha Christian University, Bandung 40164, Indonesia
[e] Physical Science and Engineering, King Abdullah University of Science and Technology, Thuwal, Saudi Arabia
[f] Geophysical Engineering Study Program, Faculty of Mining and Petroleum Engineering, Institut Teknologi Bandung, Bandung, 40132, Indonesia
[g] Department of Earth Science, University of Bergen, Allègaten 41, 5007 Bergen, Norway

ARTICLE INFO

Keywords:
Kajai Fault
Earthquake
Relocation
Focal mechanism
Rupture
Stress-change

ABSTRACT

A destructive earthquake (Mw 6.1) struck Pasaman, West Sumatra, Indonesia, on 25 February 2022, resulting in at least 18 deaths and damage to 1765 buildings. Our relocated foreshock, mainshock, and aftershocks and their source mechanisms reveal a previously unknown ~20 km long segment of the Sumatran Fault as a result of dextral strike-slip motion (strike N132°E and dip 72°SW) along what we have called the Kajai Fault. The inverted rupture model indicates a single, compact asperity with an approximate depth range of 2–11 km. This asperity extends ~14 km along strike, and ~9 km in the down-dip direction. The Coulomb stress change of the mainshock shows that areas to the north and south experienced an increase in stress, which is consistent with the observed aftershock pattern. The nearby Great Sumatran Fault segments (Angkola and Sumpur) experienced a significant increase in stress without any accompanying aftershocks, which likely increases the risk of them rupturing in the future.

1. Introduction

On February 25th, 2022, an Mw 6.1 earthquake occurred at 01:39 UTC to the west of Pasaman, West Sumatra, Indonesia (see yellow star in Fig. 1). This event was preceded by an Mw 5.1 foreshock on the same day at 01:35 UTC (Fig. 2). The Meteorological, Climatological, and Geophysical Agency/Badan Meteorologi, Klimatologi, dan Geofisika (BMKG) reported the impact of the earthquake, which measured as high as VI on the Modified Mercalli Intensity (MMI) scale in the Pasaman region; it was also measured at II on the MMI scale in nearby Malaysia (http://shakemap.bmkg.go.id/ (last accessed 7 March 2022). The earthquake damaged 1765 houses and caused at least 18 fatalities in West Sumatra Province (https://www.bnpb.go.id/ (last accessed 7 March 2022). Over the past five decades, there have been four deadly Mw > 6.0 earthquakes in the neighbourhood of Pasaman (see red stars in Fig. 1), with the three prior to the 2022 event including (1) Mw 6.1 (8 March 1977) Sumatran fault event (Hurukawa et al., 2014); (2) the Mw 6.4 (6 March 2007) doublet earthquake also on the Sumatran fault, which resulted in >70 casualties (Natawidjaja et al., 2007), and (3) Mw 7.6 (30 September 2009) intra-slab Padang earthquake, which resulted in 1117 casualties (Chian et al., 2019).

The Andaman-Sumatra-Java forearc zone extends >4000 km along the boundary between the converging Indo-Australian Plate and the Eurasian Plate. The convergence rate is not uniform and varies between 44 mm/yr in the Andamans, 60 mm/yr in southern Sumatra, and 68 mm/yr in southern Java (DeMets et al., 2010). The subduction zone to

* Corresponding author at: Department of Earth Sciences – Bullard Labs, University of Cambridge, Cambridge CB30EZ, United Kingdom.
E-mail address: ps900@cam.ac.uk (P. Supendi).

https://doi.org/10.1016/j.pepi.2022.106973
Received 2 April 2022; Received in revised form 20 October 2022; Accepted 7 December 2022
Available online 9 December 2022

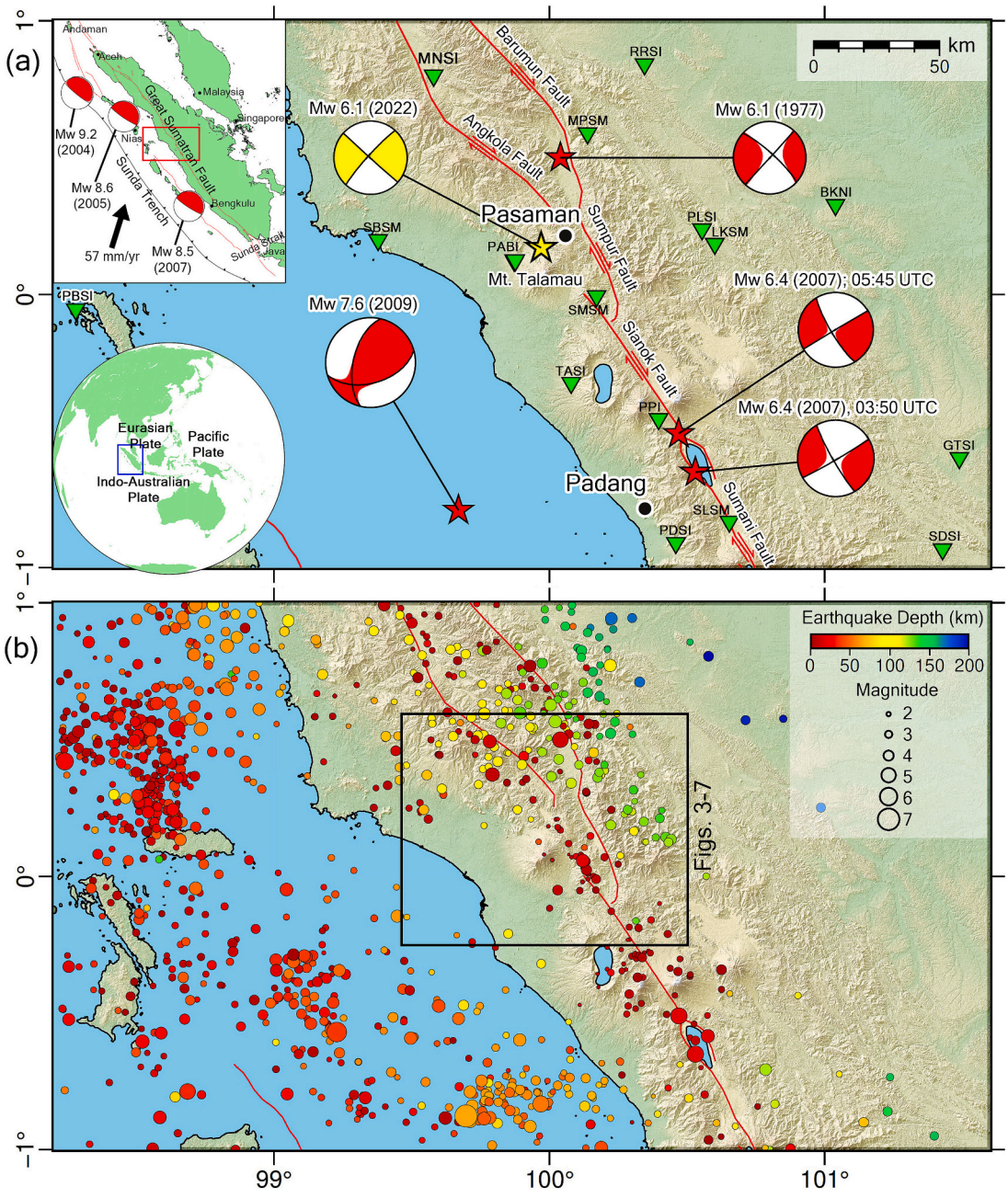

Fig. 1. (a) Map of the study area. The yellow star depicts the 25 February 2022 (Mw 6.1) mainshock and its source mechanism from BMKG (http://repogempa.bmkg.go.id/repo_new/). Green inverted triangles depict the location of BMKG seismic stations used in this study. Red lines correspond to major crustal faults in the region extracted from Irsyam et al. (2017). Historical destructive earthquakes (Mw > 6.0) in the region are denoted by red stars with source mechanisms from the global CMT catalogue (https://www.globalcmt.org/CMTsearch.html). The lower left inset shows the location of the Sumatra region (blue rectangle) with respect to Southeast Asia. The upper left inset shows the location of the study area (red rectangle) with respect to Sumatra, with source mechanisms depicting the location of three deadly Mw > 8.0 earthquakes that have occurred on the Sumatra megathrust; (b) Background seismicity in the study region from 1963 to January 2021 according to the International Seismological Centre (ISC) and BMKG earthquake catalogue, The black rectangle shows the map regions of Figs. 3-7. (For interpretation of the references to colour in this figure legend, the reader is referred to the web version of this article.)

the southwest of Sumatra features oblique convergence along a megathrust (Fitch, 1972), which has yielded three deadly Mw > 8.0 earthquakes in the decade following the turn of the 21st century, i.e. the Mw 9.2 Aceh earthquake (26 December 2004), the Mw 8.6 Nias earthquake (28 March 2005), and the Mw 8.5 Padang earthquake (12 September 2007) (see upper left inset map in Fig. 1).

Structural control of the Sumatra mainland is dominated by the Great Sumatran Fault, which extends from the Andaman transform fault system in the north to the Sunda Strait in the south (Sieh and Natawidjaja, 2000), with a recent study suggesting that it consists of 40 separate segments (Irsyam et al., 2017). Several previous studies have investigated seismic activity along the Great Sumatran Fault in the neighbourhood of our target area; for instance, Weller et al. (2012) detected several small earthquake clusters between April 2008 and February 2009 using a dense local network along the Great Sumatra Fault. One cluster, at a depth of between ~5–12 km, is in the proximity of the 2022 event. In other examples, Muksin et al. (2019) and Muksin et al. (2013) investigated seismic activity across a broad depth range in northern Sumatra, which is north of the duplex structure of the Great Sumatran fault in the central part of Sumatra.

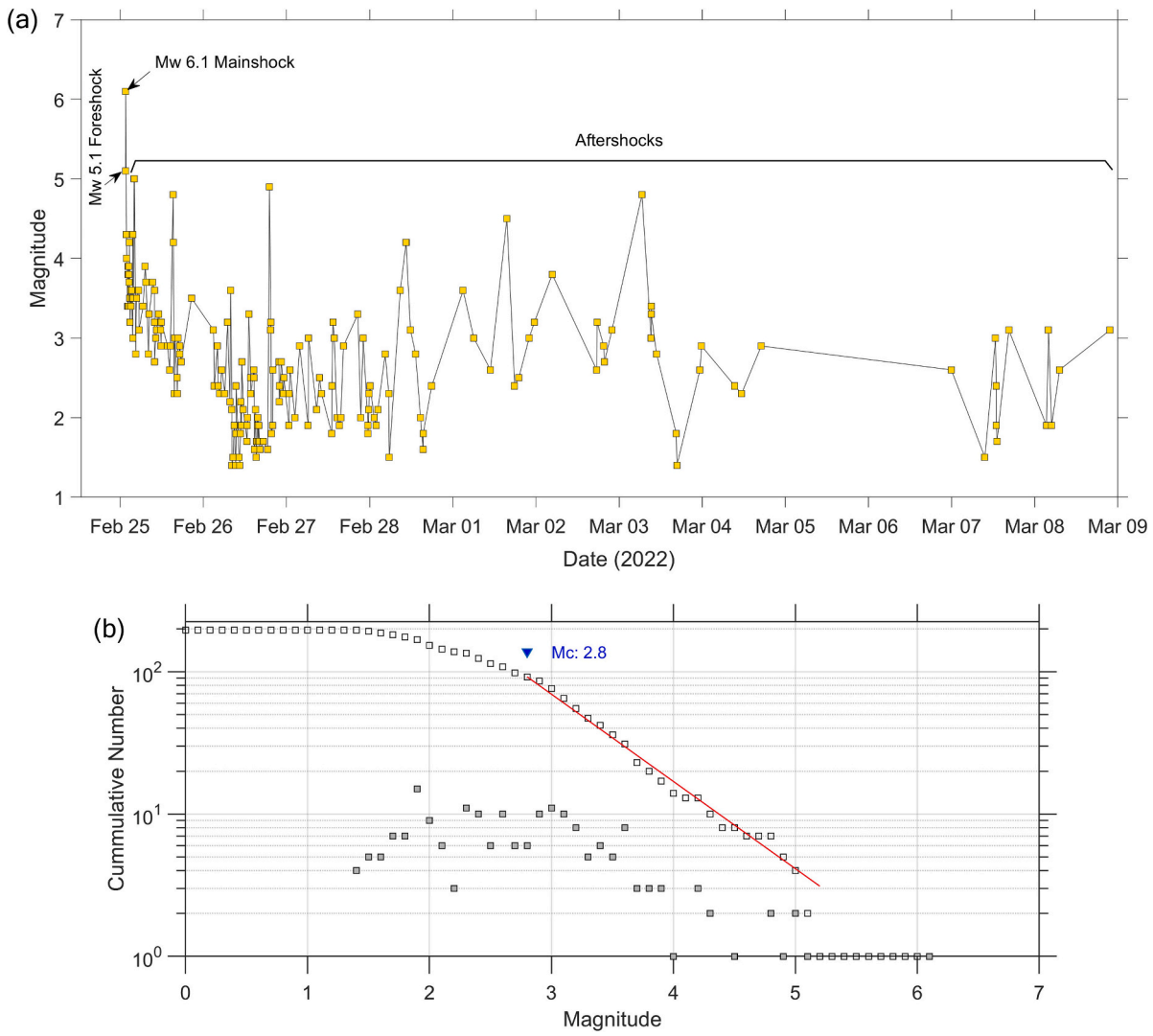

Fig. 2. (a) Plot showing magnitude vs time for the Mw 5.1 foreshock, Mw 6.1 mainshock and associated aftershocks; (b) frequency magnitude distribution (FMD), Mc = magnitude of completeness, and gray and white boxes denote discrete and cumulative events respectively.

While the behavior of this fault is relatively well understood (Burton and Hall, 2014; Fernández-Blanco et al., 2016; Natawidjaja, 2018; Salman et al., 2020), the Mw 6.1 Pasaman earthquake was not located along any of its recognized segments. The purpose of this study, therefore, is to analyse the 2022 (Mw 6.1) Pasaman earthquake and its associated foreshock and aftershock sequences through hypocenter relocation, focal mechanism solutions, and analysis of fault rupture processes and stress changes; such an analysis will provide insight into whether a previously undiscovered segment of the Great Sumatran Fault ruptured, or whether a different – but also unknown – fault was responsible.

2. Data and method

The arrival time dataset used in this study spans February 25 to March 8, 2022, and was sourced from permanent BMKG seismic network stations in West Sumatra (Fig. 1). A total of 201 earthquakes with a magnitude range of M 1.4 to M 6.1 were detected (including a foreshock, the mainshock, and aftershocks) (Fig. 2) based on the extraction of 2798 P-wave and 1067 S-wave arrival times from 16 seismic stations (see green inverted triangles in Fig. 1). The initial hypocenters from the BMKG catalogue were computed using the LocSAT linearized inversion scheme (Bratt and Nagy, 1991) included in the SeisComP3 program (Hanka et al., 2010) in the presence of the IASP91 reference velocity model (Kennett and Engdahl, 1991).

To relocate hypocenters, we employ the double difference method (Waldhauser and Ellsworth, 2000) via the HypoDD program (Waldhauser, 2001). This method is based on the assumption that the distance between earthquake pairs is small in comparison to the distance to the seismometer that recorded them, thus validating the assumption that the corresponding raypaths follow the same trajectory. P and S-wave arrival-time catalogue data for each event are searched to find paired events with similar travel-times. The maximum hypocentral separation is set to 40 km, the maximum number of neighbours per event to 60, and the minimum number of links required to define neighbours to 10. We set a maximum distance of 160 km between cluster centroid and station. These input parameter selections are made following extensive testing to determine the combination of values that produced the best results, assuming that the final distribution of relocated hypocenters does not change significantly over a reasonable range of input values. We use a 1-D velocity model derived from CRUST 1.0 (Laske et al., 2013) in the region of interest. CRUST 1.0 was built on a one-degree grid and is based on a database of crustal thicknesses derived from active source seismic and receiver function studies.

Similar to the paper by Supendi et al. (2019, 2021), we evaluate location uncertainty using a statistical resampling scheme that is based

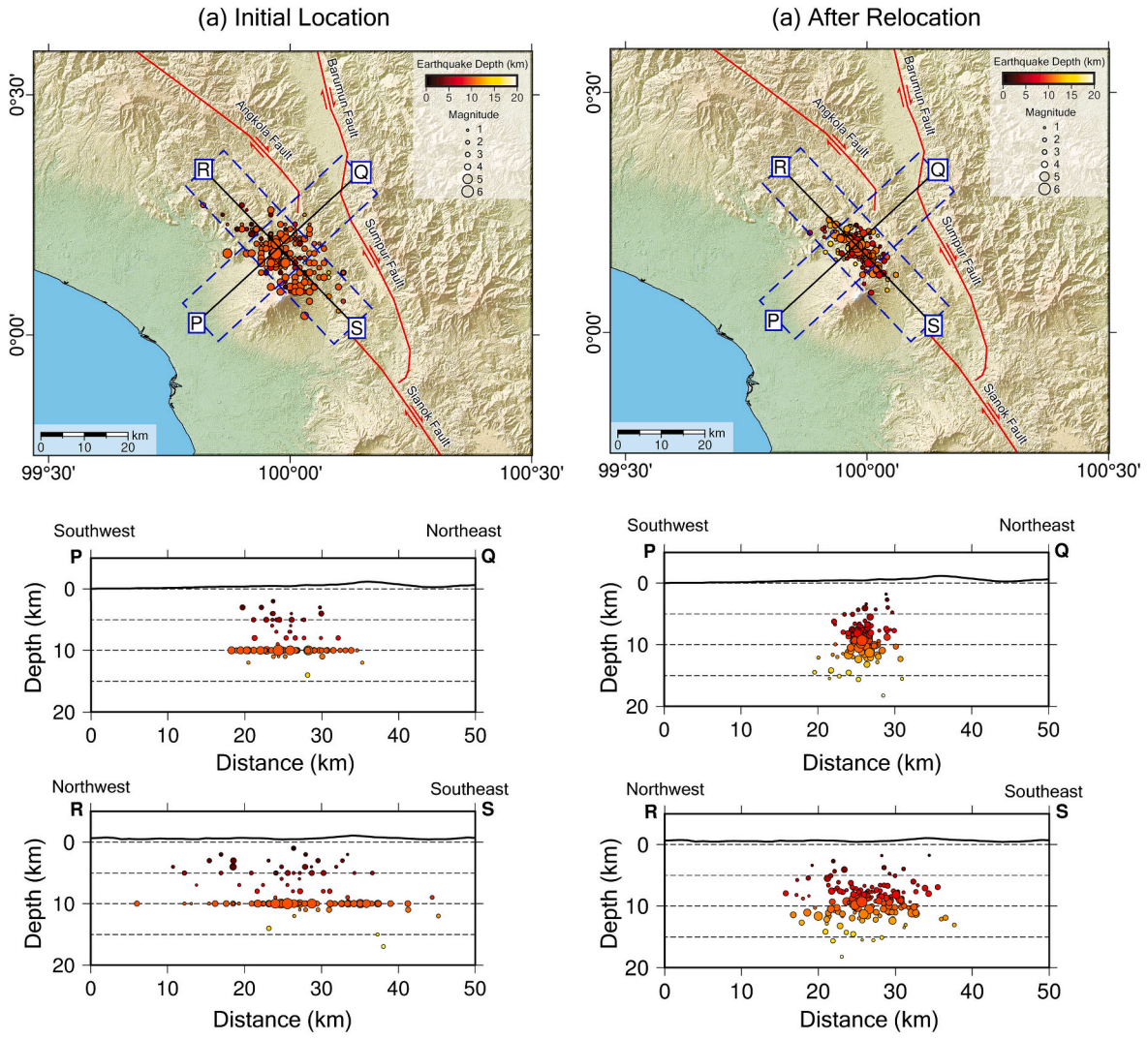

Fig. 3. Map view and vertical cross sections showing the earthquake sequence. (a) Initial location from the BMKG catalogue; (b) after relative relocation using hypoDD (196 events in total).

on the "bootstrap" method (Billings, 1994; Efron, 1982; Shearer, 1997). We used the final hypocenters to draw a random sample (with replacement) from the full set of observed residuals and used that sample to replace each measurement. The re-sampled dataset was then used to re-locate the events, and the resultant shifts in location were examined. During this process, 200 iterations were carried out. In Fig. 4, the cumulative result is shown with error ellipses containing approximately 95% of the 200 points (for each event) calculated from the bootstrap locations.

To reveal the source mechanism of the Mw 5.1 foreshock, Mw 6.1 mainshock, and two Mw 5.0 aftershocks, we invert for the moment tensor solution using Kiwi Tools (Heimann, 2011). We use seismic waveforms defined by three unrotated components (Vertical, NS, and EW) from the BMKG stations in Sumatra at epicentral distances up to 500 km. We used the amplitude spectra in a frequency domain inversion to constrain two possible nodal planes, scalar moment and improved centroid depth (Cesca et al., 2010). A frequency range of 0.01–0.08 Hz was applied for the foreshock, 0.01–0.07 Hz for the mainshock, and 0.01–0.08 Hz for the aftershocks. In this study, we find that it is necessary to use relatively long period data to achieve a reliable inversion process and reduce the influence of crustal heterogeneity (Cesca et al., 2014; Heimann, 2011). The synthetic displacement waveforms were generated in the presence of the IASP91 reference velocity model (Kennett et al., 1995).

In order to constrain the finite fault rupture modelling, we exploit teleseismic surface and body waves. We retrieved Global Seismographic Network (GSN) teleseismic broadband data from the IRIS (Incorporated Research Institutions for Seismology) Data Management Center (DMC). The raw data were corrected with their instrument responses and converted into displacement seismograms. We selected seismograms with high signal-to-noise ratios (SNR) and that provided good azimuthal coverage, which resulted in 41 P-wave seismograms, 36 SH-waves seismograms, 37 Rayleigh-wave seismograms, and 22 Love-wave seismograms. We band-pass filtered the seismograms in the frequency range 0.01 to 1 Hz for body waves, and 0.004 to 0.006 Hz for the surface waves (Sianipar et al., 2022b). In our inversion, teleseismic SH-wave seismograms receive half the weight of teleseismic P-waves because SH-waves often have a lower signal-to-noise ratio and greater arrival time pick uncertainties. Teleseismic surface waves (Rayleigh and Love wave) seismograms receive twice the weight of teleseismic P waves because Green's functions for long-period surface waves are more reliable than for body waves (e.g., Shao et al., 2011; Goldberg et al., 2020).

We performed finite-fault rupture inversion using the methods described in Ji et al. (2003, 2002); Shao et al. (2011); Twardzik and Ji (2015). The inversion is performed in the wavelet domain using a simulated annealing algorithm in order to search for the best estimates of the source model. We chose the southwest-dipping fault based on the moment tensor inversion and aftershock distribution (e.g., Supendi

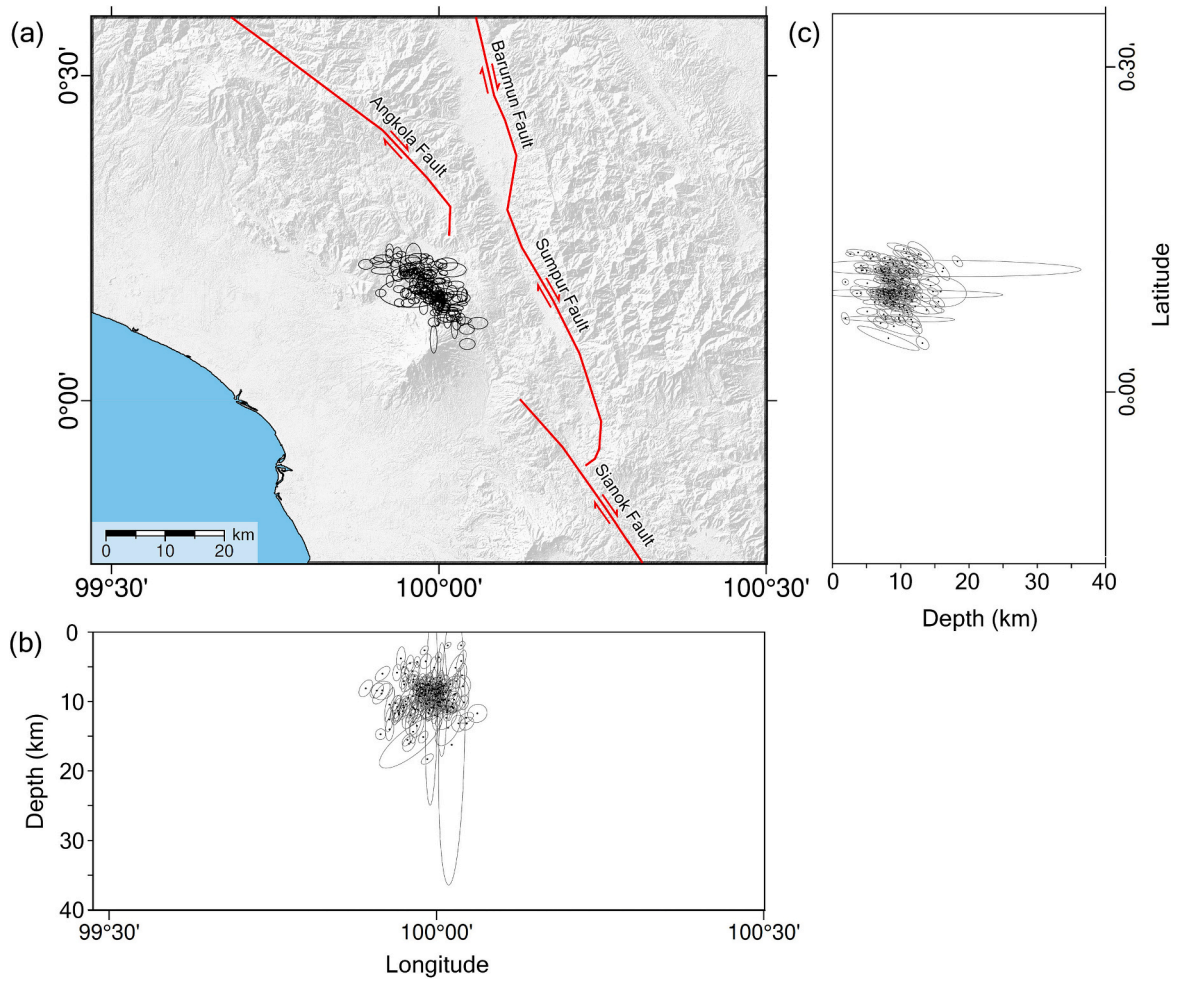

Fig. 4. (a) Map view of relative location error ellipsoids at the 95% confidence level estimated for each of the earthquakes in the sequence; (b) longitude slice; and (c) latitude slice.

et al., 2021, 2022). We divided the finite-fault plane into 42 subfault grids, each of size 3.5 km along strike and 2.2 km along dip. We set the rupture to be initiated from the relocated hypocenter (99.980°E, 0.178°N, depth 9.3 km). We search for the maximum rise time (local slip duration) of each subfault in the range 0.8 s to 3.2 s. We allow the rupture velocity to vary in the range 1.0 to 3.0 km/s, with a starting value of 2.0 km/s based on temporal constraints that overcome the intrinsic trade-off between rupture initiation time and starting time at each subfault as explained in Shao et al. (2011), and we search the rake angle (slip vector) in the range 90° to 270°. The Green's functions were computed using CRUST 1.0 (Laske et al., 2013) in the crust and PREM (Dziewonski and Anderson, 1981) below the Moho. Based on the inverted finite fault model, we determined the Coulomb static stress change (King et al., 1994) of the co-seismic slip using AutoCoulomb (Wang et al., 2021), assuming an apparent friction coefficient of 0.4 (Wang et al., 2021).

3. Result and discussion

3.1. Earthquake relocation

We relocated a foreshock, a mainshock, and 196 aftershocks related to the 2021 Pasaman earthquake from 25 February to 8 March 2022 (the remaining five were located above the surface, and therefore discarded). We compare the relocated events and initial locations (as provided by the BMKG catalogue) in both map and cross-section view (Fig. 3a), which demonstrate that the events that had previously been held at a fixed depth are now satisfactorily relocated (Fig. 3b). The travel-time residuals after HypoDD relocation clearly decrease (see supplementary Fig. S1), suggesting that the updated locations are more robust. We note that the use of the IASP91 model for the initial location undertaken by BMKG may result in the centroid of the cluster of events we consider to be mislocated, particularly in depth. However, even though HypoDD is primarily regarded as a relative relocation technique, it is able to improve on absolute locations, as demonstrated by Waldhauser (2014). Of course, the choice of velocity model used in HypoDD also matters, so we have tested our location results against those obtained using an identical workflow but with the 1-D reference model of Weller et al. (2012). The results (see Fig. S2) show a nearly identical pattern of events, but with a slight shallowing of the cluster centroid. This suggests that our results are robust, but as expected the uncertainties in depth are greater than in the horizontal dimensions.

The results from the bootstrap analysis method (see Section 2) reveal average horizontal and vertical mislocations of 0.5 km and 0.8 km respectively. The corresponding maximum mislocations in the east-west, north-south, and depth directions are 2.7 km, 1.2 km, and 10 km, respectively (Fig. 4 and Supplementary Fig. S3). Due to the assumptions inherent to our analysis of location uncertainty, the results should be considered to be more meaningful in a relative rather absolute sense.

The distribution of relocated aftershocks extends ~20 km from the northwest to the southeast in a band that is parallel to the Great Sumatran fault (Fig. 5), suggesting that it is a newly identified segment, which we call the Kajai Fault (see dashed green line in Fig. 5). This

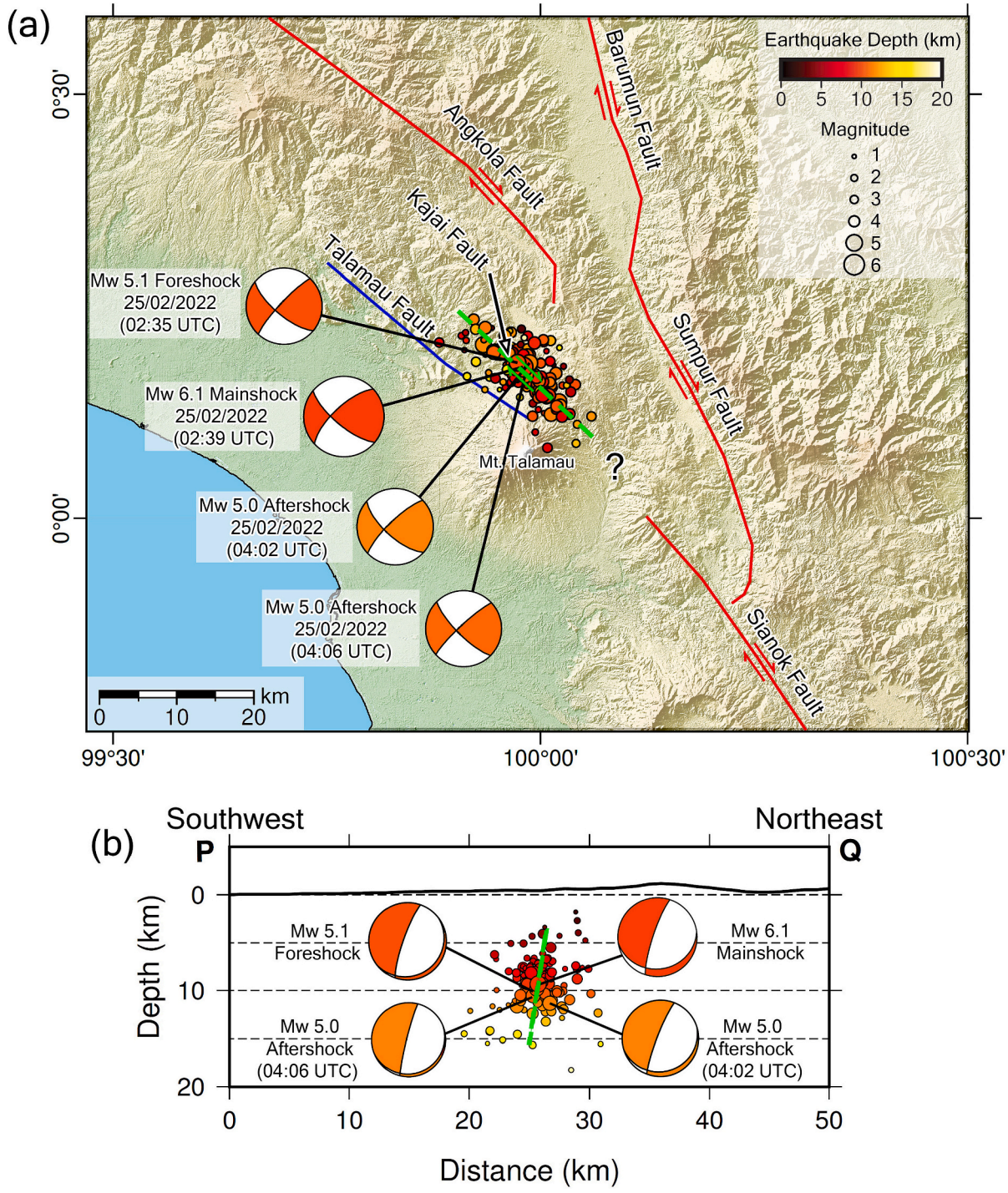

Fig. 5. (a) Map view of relocated events and focal mechanism solutions for the Mw 5.1 foreshock, Mw 6.1 mainshock, and associated aftershocks. The dashed green line denotes the approximate location and sense of movement along the fault, based on the aftershock distribution and focal mechanims. Red lines correspond to major crustal faults in the region extracted from Irsyam et al. (2017) and the blue line denotes the Talamau Fault, as extracted from Lumbanbatu (2009); (b) Southwest-Northeast cross-section illustrating how the Kajai Fault is related to the observed earthquake sequence. Focal mechanisms are plotted in a lower hemisphere projection. Each focal mechanism solution indicates a NW-SE oriented fault plane which dips to the southwest at high angle. (For interpretation of the references to colour in this figure legend, the reader is referred to the web version of this article.)

previously unidentified fault lies within a broader region targeted by several previous studies that investigated active faults using data from a temporary array (e.g., Weller et al. (2012); Lange et al. (2018)). However, due limited seismic activity during its deployment period (2008–2009), the possible presence of the Kajai Fault was not discussed. It is clear that the relocated foreshock, mainshock, and aftershocks are not located on any previously identified fault, but instead located between the Talamau fault and Angkola Fault. The existence of the Kajai Fault is also supported by the surface morphology (Fig. S4). The surface trace of the fault extends in the NW-SE direction and is aligned with the elongation of the relocated foreshock, mainshock, and aftershocks. A study of shear wave splitting by Collings et al. (2013) in the vicinity of the Kajai fault shows that the fast axis orientation of anisotropy is NW-SE, parallel to the Great Sumatran fault. This indicates the Kajai

Table 1
Focal mechanism solution data for the four earthquakes that correspond to the faults that are interpreted.

Date	Time (UTC)	Lon. (deg)	Lat. (deg)	Depth (km)	Mw	Strike (deg)	Dip (deg)	Rake (deg)	DC (%)	CLVD (%)	Event
2/25/2022	1:35:50	0.18331	99.9733	9.85	5.1	130	71	171	88	12	Foreshock
2/25/2022	1:39:28	0.17843	99.9795	9.31	6.1	130	72	159	95	5	Mainshock
2/25/2022	4:02:19	0.18311	99.9872	11.35	5.0	132	69	167	89	11	Aftershock
2/25/2022	4:06:38	0.16944	99.9823	10.51	5.0	135	76	172	85	15	Aftershock

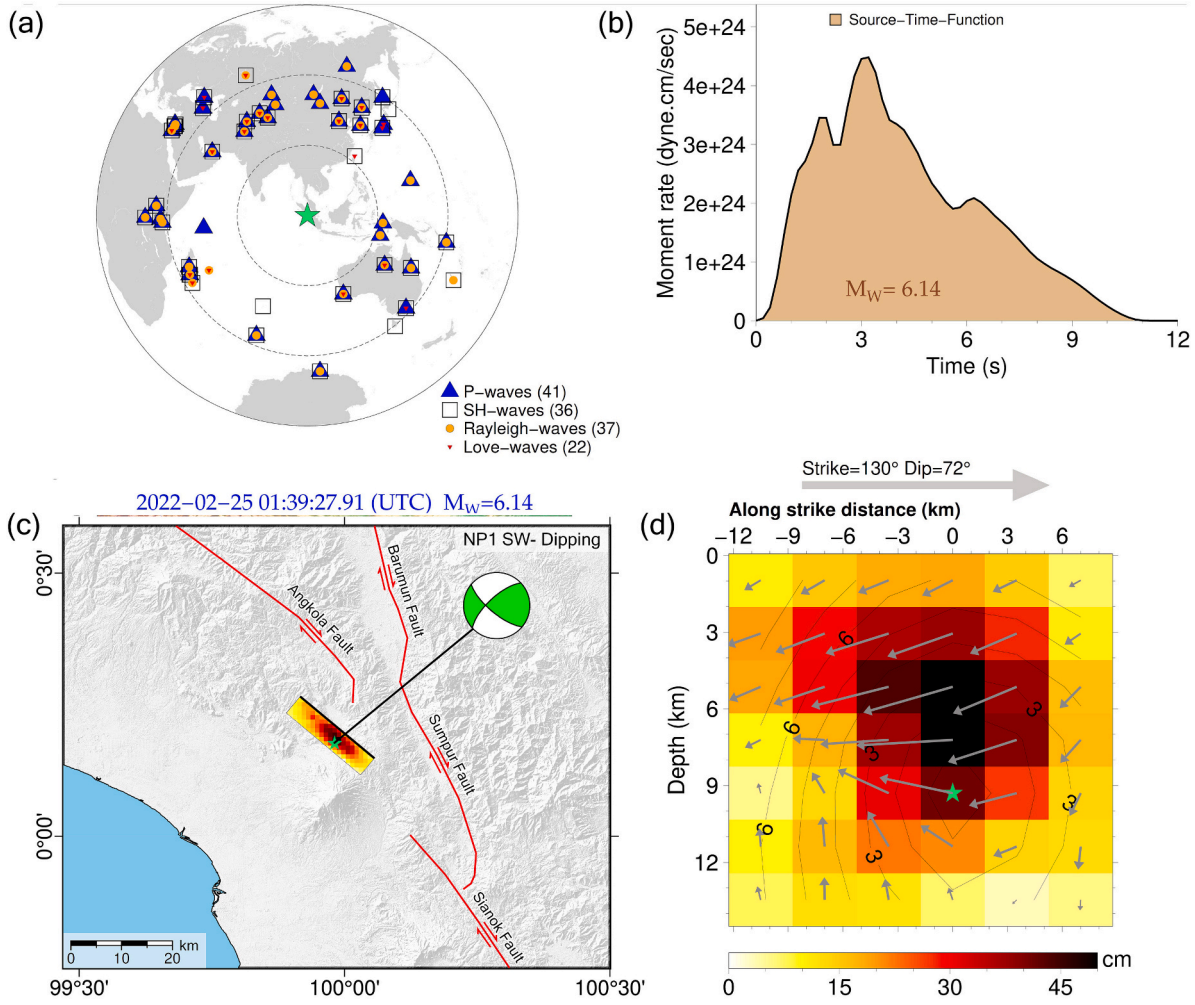

Fig. 6. (a) Teleseismic stations used to constrain source rupture model; (b) moment rate function; (c) surface projection of the coseismic slip distribution; and (d) cross-section of slip distribution in the strike direction; the gray arrows indicate the slip (rake) direction while the numbers (e.g., 3 and 6) indicate the rupture propagation time in seconds. The colour represents the co-seismic slip in cm.

Fault may also be considered a conjugate fault of the Great Sumatran fault that is currently active.

3.2. Focal mechanisms

The observed versus synthetic traces following inversion for the foreshock, mainshock, and two aftershock focal mechanisms has a misfit <0.45, indicating an adequate fit according to the criterion of Cesca et al. (2013). Our moment tensor inversion recovers solutions that are nearly 89% double-couple on average (see Table 1), suggesting that the focal mechanisms are well resolved, as supported by the plots in Fig. 3 and Figs. S5-S7. Note that if we increase the upper frequency of our bandpass filter, then the effects of small-scale heterogeneity not accounted for in our velocity model can degrade our moment tensor solutions. For example, using an upper frequency of 0.15 Hz produces solutions that are 75% double couple, while an upper frequency of 1.5 Hz yields solutions that are around 50% double couple (see Fig. S8 in the Supplementary Information).

Based on the aftershock distribution, the actual fault plane is interpreted to be the nodal plane that corresponds to the right-lateral fault with an average strike of N132°E, and dip 72°SW (Table 1). Interestingly, this fault dip is not vertical, something that Muksin et al. (2019) also found with seismicity distributions in North Sumatra.

3.3. Finite Fault model

The inverted seismic moment is approximately 2.08 × 10^{18} Nm, equivalent to moment magnitude M_W 6.14 (Fig. 6). This up-dip rupture propagation had an average speed of about 1.5 km/s, and the rupture duration is about 10 s. From our modelling, we determine that the asperity (high slip region) exhibits an average coseismic slip of ~25 cm, which is about 50% of the peak slip (53 cm) that was located at a depth

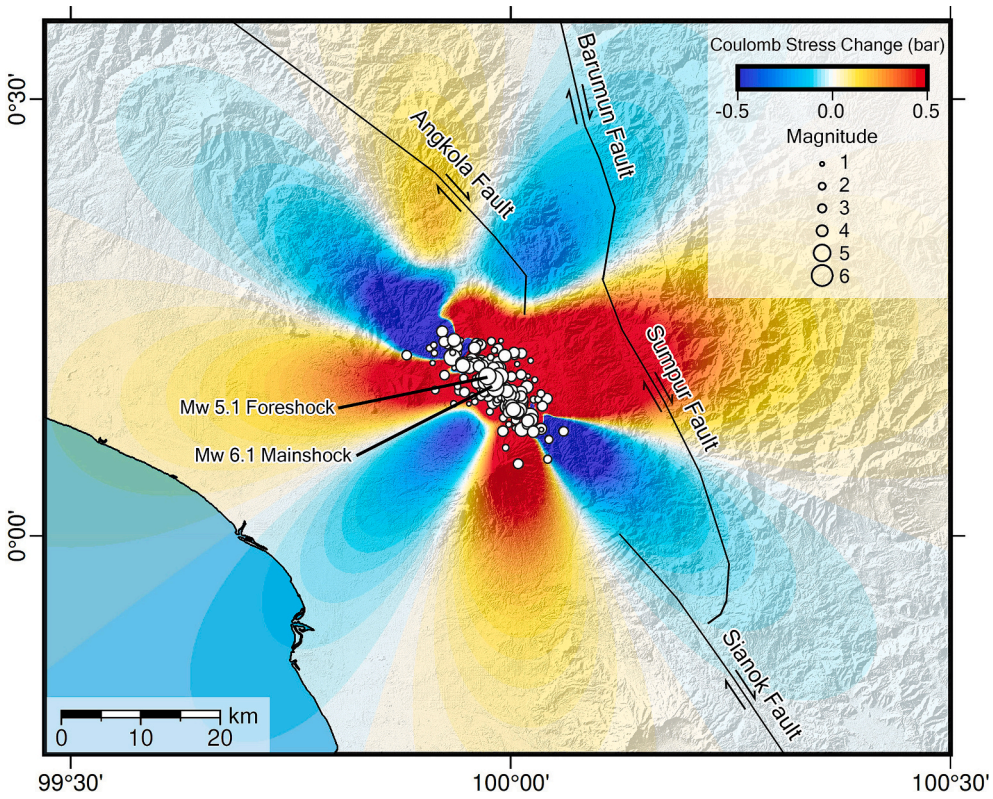

Fig. 7. Modeled Coulomb stress change caused by the Mw 6.1 Pasaman earthquake. We calculated stress changes for a fault with similar geometry to the mainshock rupture plane (strike N130°E, dip 72° SW). The blue and red colors depict negative and positive Coulomb stress changes, respectively. The white circles denote the foreshock, mainshock, and aftershocks. (For interpretation of the references to colour in this figure legend, the reader is referred to the web version of this article.)

of 7.2 km. The inverted rupture model indicates a single, compact asperity with a depth range of 2–11 km, an along-strike extension of ~14 km, and a down-dip extension of ~9 km (Fig. 6). We use a 15% peak slip (Ye et al., 2016; Sianipar et al., 2022a, 2022b) as the threshold to determine the asperity rupture area. This asperity (high slip region) is located northwest of the initial break, in the northern region of Mt. Talamau. We acknowledge that the finite-fault inversion approach used in this study has some limitations, especially when there is an absence of local/near-field and/or geodetic data, which will contribute to solution non-uniqueness (e.g., López-Comino et al., 2015). In this study, we use a 1-D radially symmetric Earth structure CRUST 1.0 (Laske et al., 2013 and PREM (Dziewonski and Anderson, 1981) to estimate the Green's function; although widely used for this purpose, it will likely add to the uncertainty in the final model.

The rupture propagated up-dip to shallower depth. The rupture extent obtained from finite-fault modelling is consistent with the aftershock distribution. Assuming that the total seismic moment depletion in this zone occurred with a circular rupture propagation, the estimate of static stress drop (Kanamori and Anderson, 1975; Supendi et al., 2021; Sianipar et al., 2022b) over the asperity is about 1.9 MPa. This low static stress drop may be related to the abundance of the aftershock productivity.

The rupture extent, foreshock, and aftershock distribution may reflect the structural control on this secondary fault segment (Salman et al., 2020). The mainshock asperity breaks the 14 km-long rupture around the hypocenter, while the aftershocks stopped expanding beyond about ~10 km to southeast and <10 km to northwest; this might suggest segmented or limited geological structure or an immature young fault segment, as shown by the cascading behavior of events (e.g., Salman et al., 2020; Sianipar et al., 2022a, 2022b). It is worth noting that such cascading behavior also occurred in the 2007 Mw 6.3 and 6.4 Lake Singkarak earthquake doublet (Daryono et al., 2012; Salman et al., 2020).

The occurrence of the Mw 5.1 foreshock (Fig. 5) and the ~2 s nucleation phase shown from the rupture model (Fig. 6) are intriguing. They occurred at the same location, in the down-dip part of the mainshock's asperity. The Mw 5.1 foreshock was located very close to the initial break of the mainshock rupture, indicating a possible stochastic process in which the mainshock is the response to a perturbation imparted by the foreshock (Gomberg, 2018; Kato and Ben-Zion, 2021). However, other conceptual models that explain the nucleation mechanism of the mainshock are also possible, such as those characterised by a deterministic pre-slip nucleation process or a progressive localization framework (Gomberg, 2018; Kato and Ben-Zion, 2021; Sianipar et al., 2022a). Previous studies have found evidence of a nucleation phase and foreshocks associated with significant earthquakes (e.g., Ellsworth and Beroza, 1995; Kato and Ben-Zion, 2021). For the case of the 2019 Mw 6.5 Ambon strike-slip rupture in eastern Indonesia, the foreshocks also occurred close to the initial break (hypocenter) of the mainshock (Sianipar et al., 2022a).

3.4. Static stress change

Static stress changes caused by the Mw 6.1 mainshock (Fig. 7) reveal areas of increased stress (depicted in red Fig. 7) in the near-field region (~ < 10 km) to the north, east, south, and west relative to the mainshock. The areas that experienced stress drops (depicted in blue) are at greater distances (~ > 10 km) from the mainshock to the northeast, southeast, southwest, and northwest. The Coulomb stress change has the potential to explain the aftershock distribution and provide insight into the possible distribution of future earthquakes (King et al., 1994; Stein and Lisowski, 1983). It is likely that the mainshock energy release immediately reduced stress at the rupture location; this stress then transferred to the northwest and southeast and caused aftershocks, since

these areas exhibit high static Coulomb stress changes. However, the high static Coulomb stress transfer (>0.5 bar) to the north and east of the mainshock requires further analysis, since the high static stress transfer may trigger a rupture of the nearby segments of the Great Sumatran Fault (Angkola and Sumpur). Furthermore, Sahara et al. (2018) suggests that the Angkola and Sumpur faults have high stress imparted by previous major events. This could produce a devastating earthquake in the future, especially if the adjacent faults are critically stressed or close to failure.

4. Conclusions

The Mw 6.1 Pasaman earthquakes were caused by slip along the newly identified and ~ 20 km long dextral strike-slip Kajai fault, which we determine to be part of the Great Sumatran Fault network. The mainshock increased stress to the north, east, south, and west, as indicated by the high Coulomb stress change in our model, which coincides with the distribution of aftershocks. However, to the north and east, there are high Coulomb stress changes unaccompanied by any aftershocks, which may increase the likelihood of a large earthquake in the Angkola and Sumpur faults. Further work is required to more firmly establish this scenario, and assess the implications of a sizable rupture along any of these faults to both people and the built environment in western Sumatra.

Data and resources

Earthquake data are available at https://doi.org/10.5281/zenodo.7096483. All figures were made using the Generic Mapping Tools (Wessel and Smith, 1998). Topography data was sourced from the Digital Elevation Model Nasional (https://tanahair.indonesia.go.id/demnas). Teleseismic waveform data was taken from the Global Seismic Networks (https://doi.org/10.7914/SN/IC; https://doi.org/10.7914/SN/II; https://doi.org/10.7914/SN/IU; https://doi.org/10.18715/GEOSCOPE.G; https://doi.org/10.14470/TR560404).

Authors' contributions

P.S., N.R., D.S., and S.W. wrote the manuscript. P.S. performed the hypocenter relocation, A.S. performed the focal mechanism analysis, and D.S. performed the source model analysis. All authors have reviewed and contributed to the preparation of the manuscript.

Declaration of Competing Interest

The authors declare that they have no known competing financial interests or personal relationships that could have appeared to influence the work reported in this paper.

Data availability

Data will be made available on request.

Acknowledgement

We thank the Agency for Meteorology, Climatology, and Geophysics (BMKG) of Indonesia for granting access to the earthquake data used in this research. This research is funded by the British Council (Newton Fund) G107511 awarded to N.R., the University of Cambridge (United Kingdom) through a Herchel Smith Research Fellowship awarded to P. S., and was supported by Konsorsium Gempabumi dan Tsunami BMKG (Indonesia).

Appendix A. Supplementary data

Supplementary data to this article can be found online at https://doi.org/10.1016/j.pepi.2022.106973.

References

Billings, S.D., 1994. Simulated annealing for earthquake location. Geophys. J. Int. 118, 680–692. https://doi.org/10.1111/j.1365-246X.1994.tb03993.x.
Bratt, S.R., Nagy, W., 1991. The LocSAT Program. Science Applications International Corporation (SAIC).
Burton, P.W., Hall, T.R., 2014. Segmentation of the Sumatran fault: Burton and Hall: segmentation of the Sumatran fault. Geophys. Res. Lett. 41, 4149–4158. https://doi.org/10.1002/2014GL060242.
Cesca, S., Heimann, S., Stammler, K., Dahm, T., 2010. Automated procedure for point and kinematic source inversion at regional distances. J. Geophys. Res. 115, B06304. https://doi.org/10.1029/2009JB006450.
Cesca, S., Braun, T., Maccaferri, F., Passarelli, L., Rivalta, E., Dahm, T., 2013. Source modelling of the M5–6 Emilia-Romagna, Italy, earthquakes (2012 May 20–29). Geophys. J. Int. 193, 1658–1672. https://doi.org/10.1093/gji/ggt069.
Cesca, S., Grigoli, F., Heimann, S., González, Á., Buforn, E., Maghsoudi, S., Blanch, E., Dahm, T., 2014. The 2013 September–October seismic sequence offshore Spain: a case of seismicity triggered by gas injection? Geophys. J. Int. 198, 941–953. https://doi.org/10.1093/gji/ggu172.
Chian, S.C., Wilkinson, S.M., Whittle, J.K., Mulyani, R., Alarcon, J.E., Pomonis, A., Saito, K., Fraser, S., Goda, K., Macabuag, J., Offord, M., Hunt-Raby, A.C., Sammonds, P., Franco, G., Stone, H., Ahmed, B., Hughes, F.E., Jirouskova, N.K., Kaminski, S., Lopez, J., 2019. Lessons Learnt From the 2009 Padang Indonesia, 2011 Tōhoku Japan and 2016 Muisne Ecuador Earthquakes. Front. Built Environ. 5, 73. https://doi.org/10.3389/fbuil.2019.00073.
Collings, R., Rietbrock, A., Lange, D., Tilmann, F., Nippress, S., Natawidjaja, D., 2013. Seismic anisotropy in the Sumatra subduction zone: SEISMIC ANISOTROPY IN SUMATRA. J. Geophys. Res. Solid Earth 118, 5372–5390. https://doi.org/10.1002/jgrb.50157.
Daryono, M.R., Natawidjaja, D.H., Sieh, K., 2012. Twin-surface ruptures of the march 2007 M>6 earthquake doublet on the Sumatran Fault. Bull. Seismol. Soc. Am. 102, 2356–2367. https://doi.org/10.1785/0120110220.
DeMets, C., Gordon, R.G., Argus, D.F., 2010. Geologically current plate motions. Geophys. J. Int. 181, 1–80. https://doi.org/10.1111/j.1365-246X.2009.04491.x.
Dziewonski, A.M., Anderson, D.L., 1981. Preliminary reference Earth model. Phys. Earth Planet. Inter. 25, 297–356. https://doi.org/10.1016/0031-9201(81)90046-7.
Efron, B., 1982. The Jackknife, the Bootstrap and Other Resampling Plans. Society for Industrial and Applied Mathematics. https://doi.org/10.1137/1.9781611970319.
Ellsworth, W.L., Beroza, G.C., 1995. Seismic Evidence for an Earthquake Nucleation Phase. Science 268, 851–855. https://doi.org/10.1126/science.268.5212.851.
Fernández-Blanco, D., Philippon, M., von Hagke, C., 2016. Structure and kinematics of the Sumatran Fault System in North Sumatra (Indonesia). Tectonophysics 693, 453–464. https://doi.org/10.1016/j.tecto.2016.04.050.
Fitch, T.J., 1972. Plate convergence, transcurrent faults, and internal deformation adjacent to Southeast Asia and the western Pacific. J. Geophys. Res. 77, 4432–4460. https://doi.org/10.1029/JB077i023p04432.
Goldberg, D.E., Melgar, D., Sahakian, V.J., Thomas, A.M., Xu, X., Crowell, B.W., Geng, J., 2020. Complex rupture of an immature fault zone: a simultaneous kinematic model of the 2019 Ridgecrest, CA earthquakes. Geophys. Res. Lett. 47 (3) https://doi.org/10.1029/2019GL086382 e2019GL086382.
Gomberg, J., 2018. Unsettled earthquake nucleation. Nat. Geosci. 11, 463–464. https://doi.org/10.1038/s41561-018-0149-x.
Hanka, W., Saul, J., Weber, B., Becker, J., Harjadi, P., GITEWS Seismology Group, 2010. Real-time earthquake monitoring for tsunami warning in the Indian Ocean and beyond. Nat. Hazards Earth Syst. Sci. 10, 2611–2622. https://doi.org/10.5194/nhess-10-2611-2010.
Heimann, S., 2011. A Robust Method to Estimate Kinematic Earthquake Source Parameters (PhD Thesis).. University of Hamburg.
Hurukawa, N., Wulandari, B.R., Kasahara, M., 2014. Earthquake history of the Sumatran Fault, Indonesia, since 1892, derived from relocation of large earthquakes. Bull. Seismol. Soc. Am. 104, 1750–1762. https://doi.org/10.1785/0120130201.
Irsyam, M., Widiyantoro, S., Natawidjaya, D.H., Meilano, I., Rudyanto, A., Hidayati, S., Triyoso, W., Hanifa, N.R., Djarwadi, D., Faizal, L., Sunarjito, S., 2017. Peta sumber dan bahaya gempa Indonesia tahun 2017. In: Pusat Penelitian dan Pengembangan Perumahan dan Permukiman, Kementerian Pekerjaan Umum dan Perumahan Rakyat.
Ji, C., Helmberger, D.V., Wald, D.J., Ma, K.-F., 2003. Slip history and dynamic implications of the 1999 Chi-Chi, Taiwan, earthquake: SLIP HISTORY OF THE 1999 CHI-CHI EARTHQUAKE. J. Geophys. Res. 108 https://doi.org/10.1029/2002JB001764.
Kanamori, H., Anderson, D.L., 1975. Theoretical basis of some empirical relations in seismology. Bull. Seismol. Soc. Am. 65, 1073–1095.
Kato, A., Ben-Zion, Y., 2021. The generation of large earthquakes. Nat Rev Earth Environ 2, 26–39. https://doi.org/10.1038/s43017-020-00108-w.
Kennett, B.L.N., Engdahl, E.R., 1991. Traveltimes for global earthquake location and phase identification. Geophys. J. Int. 105, 429–465. https://doi.org/10.1111/j.1365-246X.1991.tb06724.x.
Kennett, B.L.N., Engdahl, E.R., Buland, R., 1995. Constraints on seismic velocities in the Earth from traveltimes. Geophys. J. Int. 122, 108–124. https://doi.org/10.1111/j.1365-246X.1995.tb03540.x.
King, G.C.P., Stein, R.S., Lin, J., 1994. Static stress changes and the triggering of earthquakes. Bull. Seismol. Soc. Am. 84, 935–953.

Lange, D., Tilmann, F., Henstock, T., Rietbrock, A., Natawidjaja, D., Kopp, H., 2018. Structure of the central Sumatran subduction zone revealed by local earthquake travel-time tomography using an amphibious network. Solid Earth 9, 1035–1049. https://doi.org/10.5194/se-9-1035-2018.

Laske, G., Masters, G., Ma, Z., Pasyanos, M., 2013. Update on CRUST1.0 – A 1-degree global model of earth's crust. Geophysical Research 15.

López-Comino, J.Á., Stich, D., Ferreira, A.M.G., Morales, J., 2015. Extended fault inversion with random slipmaps: a resolution test for the 2012 M w 7.6 Nicoya, Costa Rica earthquake. Geophys. J. Int. 202, 1505–1521. https://doi.org/10.1093/gji/ggv235.

Lumbanbatu, U.M., 2009. Morfogenetik daerah Lubuksikaping provinsi Sumatera Barat. Jurnal Geologi dan Sumberdaya Mineral 19 (2).

Muksin, U., Bauer, K., Haberland, C., 2013. Seismic Vp and Vp/vs structure of the geothermal area around Tarutung (North Sumatra, Indonesia) derived from local earthquake tomography. J. Volcanol. Geotherm. Res. 260, 27–42. https://doi.org/10.1016/j.jvolgeores.2013.04.012.

Muksin, U., Bauer, K., Muzli, M., Ryberg, T., Nurdin, I., Masturiyono, M., Weber, M., 2019. AcehSeis project provides insights into the detailed seismicity distribution and relation to fault structures in Central Aceh, Northern Sumatra. J. Asian Earth Sci. 171, 20–27. https://doi.org/10.1016/j.jseaes.2018.11.002.

Natawidjaja, D.H., 2018. Updating active fault maps and sliprates along the Sumatran Fault Zone, Indonesia. IOP Conf. Ser.: Earth Environ. Sci. 118, 012001 https://doi.org/10.1088/1755-1315/118/1/012001.

Natawidjaja, D.H., Tohari, A., Subowo, E., Daryono, M.R., 2007. Western Sumatra Earthquakes of 6 March 2007 (Special Earthquake Report No. 5 pp). EERI.

Sahara, D.P., Widiyantoro, S., Irsyam, M., 2018. Stress heterogeneity and its impact on seismicity pattern along the equatorial bifurcation zone of the Great Sumatran Fault, Indonesia. J. Asian Earth Sci. 164, 1–8. https://doi.org/10.1016/j.jseaes.2018.06.002.

Salman, R., Lindsey, E.O., Feng, L., Bradley, K., Wei, S., Wang, T., Daryono, M.R., Hill, E. M., 2020. Structural controls on rupture extent of recent Sumatran fault zone earthquakes, Indonesia. J. Geophys. Res. Solid Earth 125. https://doi.org/10.1029/2019JB018101.

Shao, G., Li, X., Ji, C., Maeda, T., 2011. Focal mechanism and slip history of the 2011 M w 9.1 off the Pacific coast of Tohoku Earthquake, constrained with teleseismic body and surface waves. Earth Planet Sp 63, 559–564. https://doi.org/10.5047/eps.2011.06.028.

Shearer, P.M., 1997. Improving local earthquake locations using the L1 norm and waveform cross correlation: application to the Whittier Narrows, California, aftershock sequence. J. Geophys. Res. 102, 8269–8283. https://doi.org/10.1029/96JB03228.

Sianipar, D., Daryono, D., Halauwet, Y., Ulfiana, E., Sipayung, R., Daniarsyad, G., Heryandoko, N., Prasetyo, R.A., Serhalawan, Y., Karnawati, D., 2022a. Intense foreshock swarm preceding the 2019 MW 6.5 Ambon (Seram, Indonesia) earthquake and its implication for the earthquake nucleation process. Phys. Earth Planet. Inter. 322, 106828 https://doi.org/10.1016/j.pepi.2021.106828.

Sianipar, D., Huang, B.-S., Ma, K.-F., Hsieh, M.-C., Chen, P.-F., Daryono, D., 2022b. Similarities in the rupture process and cascading asperities between neighboring fault patches and seismic implications: the 2002–2009 Sumbawa (Indonesia) earthquakes with moment magnitudes of 6.2–6.6. J. Asian Earth Sci. 229, 105167 https://doi.org/10.1016/j.jseaes.2022.105167.

Sieh, K., Natawidjaja, D., 2000. Neotectonics of the Sumatran fault, Indonesia. J. Geophys. Res. 105, 28295–28326. https://doi.org/10.1029/2000JB900120.

Stein, R.S., Lisowski, M., 1983. The 1979 Homestead Valley Earthquake Sequence, California: control of aftershocks and postseismic deformation. J. Geophys. Res. 88, 6477. https://doi.org/10.1029/JB088iB08p06477.

Supendi, P., Nugraha, A.D., Widiyantoro, S., Abdullah, C.I., Puspito, N.T., Palgunadi, K. H., Daryono, D., Wiyono, S.H., 2019. Hypocenter relocation of the aftershocks of the Mw 7.5 Palu earthquake (September 28, 2018) and swarm earthquakes of Mamasa, Sulawesi, Indonesia, using the BMKG network data. Geosci. Lett. 6, 18. https://doi.org/10.1186/s40562-019-0148-9.

Supendi, P., Ramdhan, M., Priyobudi Sianipar, D., Wibowo, A., Gunawan, M.T., Rohadi, S., Riama, N.F., Daryono Prayitno, B.S., Murjaya, J., Karnawati, D., Meilano, I., Rawlinson, N., Widiyantoro, S., Nugraha, A.D., Marliyani, G.I., Palgunadi, K.H., Elsera, E.M., 2021. Foreshock–mainshock–aftershock sequence analysis of the 14 January 2021 (Mw 6.2) Mamuju–Majene (West Sulawesi, Indonesia) earthquake. Earth Planets Space 73, 106. https://doi.org/10.1186/s40623-021-01436-x.

Supendi, P., Sianipar, D., Widiyantoro, S., Rawlinson, N., Daryono Prayitno, B.S., Gunawan, M.T., Sadly, M., Karnawati, D., Nugraha, A.D., Palgunadi, K.H., Muttaqy, F., Rahayu, T., 2022. Analysis of the April 10, 2021 (Mw 6.1) destructive intra-slab earthquake, East Java, Indonesia. Phys. Earth Planet. Inter. 326, 106866 https://doi.org/10.1016/j.pepi.2022.106866.

Twardzik, C., Ji, C., 2015. The Mw7.9 2014 intraplate intermediate-depth Rat Islands earthquake and its relation to regional tectonics. Earth Planet. Sci. Lett. 431, 26–35. https://doi.org/10.1016/j.epsl.2015.08.033.

Waldhauser, F., 2001. hypoDD-A Program to Compute Double-Difference Hypocenter Locations (Report No. 2001–113). https://doi.org/10.3133/ofr01113.

Waldhauser, F., 2014. Hanford Site-Wide Probabilistic Seismic Hazard Analysis (PSHA): High-Resolution Seismicity Analysis of the Yakima Fold and Thrust Belt Region, Washington, Hanford PSHA Seismicity Analysis, No. 209054. https://www.hanford.gov/files.cfm/Appendix_F21.pdf.

Waldhauser, F., Ellsworth, W.L., 2000. A double-difference earthquake location algorithm: method and application to the northern Hayward fault, California. Bull. Seismol. Soc. Am. 90, 1353–1368. https://doi.org/10.1785/0120000006.

Wang, J., Xu, C., Freymueller, J.T., Wen, Y., Xiao, Z., 2021. AutoCoulomb: an automated configurable program to calculate coulomb stress changes on receiver faults with any orientation and its application to the 2020 mw 7.8 Simeonof Island, Alaska, Earthquake. Seismological Research Letters 92, 2591–2609. https://doi.org/10.1785/0220200283.

Weller, O., Lange, D., Tilmann, F., Natawidjaja, D., Rietbrock, A., Collings, R., Gregory, L., 2012. The structure of the Sumatran Fault revealed by local seismicity: THE STRUCTURE OF THE SUMATRAN FAULT. Geophys. Res. Lett. 39, n/a-n/a. https://doi.org/10.1029/2011GL050440.

Wessel, P., Smith, W.H.F., 1998. New, improved version of generic mapping tools released. Eos, Transactions American Geophysical Union 79, 579. https://doi.org/10.1029/98EO00426.

Ye, L., Lay, T., Kanamori, H., Rivera, L., 2016. Rupture characteristics of major and great (Mw≥ 7.0) megathrust earthquakes from 1990 to 2015: 1. Source parameter scaling relationships. J. Geophys. Res. Solid Earth 121 (2), 826–844. https://doi.org/10.1002/2015JB012426.